WANG, S., WANG, C., TAKYI-ANINAKWA, P., JIN, S., FERNANDEZ, C. and HUANG, Q. 2024. An improved parameter identification and radial basis correction-differential support vector machine strategies for state-of-charge estimation of urban-transportation-electric-vehicle lithium-ion batteries. *Journal of energy storage* [online], 80, article number 110222. Available from: https://doi.org/10.1016/j.est.2023.110222

An improved parameter identification and radial basis correction-differential support vector machine strategies for state-of-charge estimation of urban-transportation-electric-vehicle lithium-ion batteries.

WANG, S., WANG, C., TAKYI-ANINAKWA, P., JIN, S., FERNANDEZ, C. and HUANG, Q.

2024

An improved parameter identification and radial basis correction-differential support vector machine strategies for state-of-charge estimation of urban-transportation-electric-vehicle lithium-ion batteries

Shunli Wang [a,b,*], Chao Wang [b], Paul Takyi-Aninakwa [b], Siyu Jin [c], Carlos Fernandez [d], Qi Huang [b]

[a] *Electric Power College, Inner Mongolia University of Technology, Inner Mongolia 010000, China*
[b] *School of Information Engineering, Southwest University of Science and Technology, Mianyang 621010, China*
[c] *Department of Energy Technology, Aalborg University, Pontoppidanstraede, 111 9220 Aalborg East, Denmark*
[d] *School of Pharmacy and Life Sciences, Robert Gordon University, Aberdeen AB10-7GJ, UK*

* Corresponding author at: School of Information Engineering, Southwest University of Science and Technology, Mianyang 621010, China.
E-mail address: wangshunli@swust.edu.cn (S. Wang).

A B S T R A C T

The State estimation and determination of time-varying model parameters are crucial for ensuring the safe management of lithium-ion batteries. This paper designs a limited memory recursive least square algorithm to improve the accuracy of online parameter identification. An adaptive radial basis correction-differential support vector machine model is constructed to correct the state of charge value by considering the dynamic characteristic parameters. It greatly reduces estimation error and noise, while monitoring the critical conditions for safe and reliable online battery operation. The estimation effects of the proposed model are verified under hybrid pulse power characterization and dynamic stress test working conditions. The maximum error values obtained are 0.037 % and 0.336 %, respectively, thus achieving high-precision estimation. The proposed method is adaptive to real-time battery management applications, laying a foundation for robust state estimation of lithium-ion batteries used in urban transportation electric vehicles.

Keywords: Lithium-ion battery; Limited memory recursive least square; Adaptive radial basis correction; Differential support vector machine; Adaptive extended Kalman filter

1. Introduction

Since combustion engine-powered vehicles are a major contributor to global warming and its effects on the environment, the development of the automotive industry is gradually shifting from internal combustion engine-powered vehicles to electric vehicles to solve energy and climate problems [1,2]. With the advancement of technology, lithium- ion batteries (LIBs) serve as one of the main components widely used in electric vehicles (EVs), smart devices, etc. due to their advantages, such as high energy density, lightweight and compact design, long cycling performance, low self-discharge rate, and no memory effect [3,4]. Therefore, LIBs have become an essential part of the new energy field, which is a key breakthrough not only in EVs but also in optimizing the existing energy storage and supply system.

Effective management by the battery management system (BMS) is critical to extending the service life and reducing costs. Also, it ensures the safety and acceptable operation of LIBs in EVs [5,6]. With the increasing demand and application of LIBs, their safety and reliable operation have become the focus of attention in all walks of life [7,8]. BMS is responsible for monitoring the real-time status of the battery, such as the state of charge (SOC), state of health (SOH), and state of power (SOP) [9]. Among the BMS functions, the SOC is a key state parameter that serves as the basis for the safe and efficient management of LIBs, which promotes BMS applications and developments.

The SOC is a measure of the ratio of the available energy to the maximum possible charge that can be stored in the battery and is determined by the BMS [10,11]. Accurate real-time estimation SOC can prevent the occurrence of hidden dangers that damage the battery cycle life and safe performance, such as overcharging and over-discharging [12]. Currently, there are three types of SOC prediction methods mainly include experimental tests, model-driven, and data-driven [13]. The experimental test-based method calculates the lithium battery SOC by measuring physical quantities such as battery voltage, current, and temperature, and then calculating the lithium battery SOC based on known physical relationships [14]. It is generally used as a calibration method for battery SOC estimation or for post-battery maintenance work.

As the SOC change is a nonlinear state parameter in the application of LIBs, there are significant difficulties in improving the estimation accuracy [15]. The model-driven approach is an indirect estimation method with mainly electrochemical models and equivalent circuit models [16]. The electrochemical model accuracy is high, which is suitable for theoretical analysis, but the model structure is too complex and has many parameters, which is extremely computationally intensive [17]. The equivalent circuit model (ECM) is simple, with few parameters, and a small amount of calculation [18], usually combined with parameter identification and state space equations to achieve the pre- diction and estimation of lithium battery-related state.

The method based on the ECM first needs to collect information such as battery voltage, current, and temperature through experiments, then establish a suitable equivalent model to construct the state space equation, carry out model parameter identification, and finally use a suitable control theory algorithm to estimate SOC [19]. Currently, the Kalman Filter (KF) is widely used. Naseri et al. proposed an enhanced equivalent circuit model based on the Wiener structure to improve the nonlinear capability of capturing LIBs [20]. The results showed that the accuracy of the EKF algorithm to estimate the SOC is improved by 1.5 % compared to the conventional second-order equivalent circuit model. Duan et al. used a robust EKF method with correlated entropy loss for SOC estimation to improve the estimation accuracy in non-Gaussian environments, and the results show that the mean square error of the proposed method is reduced by 0.849 % [21]. Wang et al. find that the deviation of OCV would affect the accuracy of SOC estimation by the EKF algorithm, and quantitatively analyzed the influence of open-circuit voltage (OCV) deviation on the accuracy of SOC estimation by the EKF algorithm [22]. Furthermore, a dynamic matrix control-extended Kalman filter (DMC-EKF) algorithm is proposed to estimate OCV and SOC. The results show that the proposed algorithm can estimate SOC more accurately, and the error is reduced by 2 % compared with the unscented Kalman filtering (UKF) algorithm.

Nomenclature

LIBs	lithium-ion batteries
EVs	electric vehicles
SOC	state of charge
SOH	state of health
SOP	state of power
BMS	battery management system
ECM	equivalent circuit model
KF	Kalman Filter
OCV	open-circuit voltage
DMC-EKF	dynamic matrix control-extended Kalman filter
UKF	unscented Kalman filtering
LSTM	long short term memory
IBMO-SVM	improved barnacle mating optimizer-support vector machine
	particle swarm optimization
DF	data-fusion
VRFBs	vanadium redox flow batteries
RBC-DSVM	radial basis correction-differential support vector machine
LMRLS	limited memory recursive least square
DST	dynamic stress test
HPPC	hybrid pulse power characterization
BBDST	Beijing bus dynamic stress test
FOT-ECM	first-order Thevenin model
R_0	internal ohmic resistance
R_p	polarization resistance
C_p	polarization capacitance
U_p	polarization voltage
I	charge-discharge current
U_{oc}	open-circuit voltage
U_L	terminal voltage
U_o	voltage across the ohmic resistance
Q_n	nominal capacity
Δk/T	the sampling interval
w	system noise
v	measurement noise
τ	polynomial coefficient
$y(k)$	output value of the system
(k)	observation vectors
$\theta(k)$	parameter vector to be estimated
$e(k)$	noise observation vector
x_k	state-transition matrix
u_k	control-input vector
$\Phi(x)$	kernel function
ε	approximate accuracy
ξ_i	relaxation variables

The data-driven method is based on using data to estimate SOC directly by mining the mapping relationship between the own characteristics of battery measurement parameters such as current, voltage, temperature, and internal resistance and the battery SOC [23–25]. Its advantage is that it does not need to build a battery model, but it must be backed by high-quality measurement data to obtain accurate estimation results. Hong et al. proposed a multi-step forward online joint SOC prediction method based on the long short term memory (LSTM) neural network and multiple linear regression algorithm, and the experimental validation showed that the method has good stability, flexibility, and robustness [26]. To overcome the shortcomings of the black box principle and thus fully exploit the performance of deep learning, Tian et al. proposed to integrate two kinds of domain knowledge into a deep learning-based approach [27]. Liu et al. proposed the improved barnacle mating optimizer-support vector machine (IBMO-SVM) model and used it for SOC estimation of LIBs [28]. The results show that the SOC estimation method proposed in this study is highly accurate and reliable.

In summary, traditional methods and their improvements are more applied and mature, such as literature [20] and literature [21]. Some researchers use an AEKF based on the correction factor of the forgetting factor recursive least-squares method to realize SOC estimation [29]. There are also some researchers using an improved particle swarm optimization (IPSO) method combined with the EKF method to realize the state parameters online estimate [30]. Zhao et al. proposed a data-fusion (DF) method to improve the accuracy of SOC estimation for vanadium redox flow batteries (VRFBs) by combining EKF and AEKF SOC estimation results. The results show that the proposed DF method exhibited high fidelity and accuracy in estimating the SOC [31]. However, the data processing cost of this method is high, and two EKFs are used. Some scholars have introduced machine learning and neural network methods for SOC estimation, such as literature [26–28]. How- ever, these networks have high complexity, poor accuracy and stability, and high application cost.

With highly nonlinear operating conditions, the acquisition and modeling of the time-varying internal parameters are essential factors affecting accurate parameterization in SOC estimation [32–34]. It is necessary to ensure the parameter acquisition of the state-space model under complex working conditions to obtain an accurate real-time SOC estimation of LIBs [35]. In this paper, an improved hybrid adaptive radial basis correction-differential support vector machine (RBC-DSVM) model is proposed for the accurate SOC estimation of LIBs. The limited memory recursive least square LMRLS) parameter identification model is designed to improve the accuracy of online parameter identification.

The SOC estimation from the AEKF method is used as input into the DSVM model with RBC iteration to correct the errors and optimize the final SOC. Finally, the SOC over the whole life cycle of the battery is accurately estimated. The SOC estimation effects are verified based on the actual working conditions, such as the dynamic stress test (DST) and hybrid pulse power characterization (HPPC). The proposed RBC-DSVM model is tested and verified under HPPC and DST working conditions with high accuracy and robustness advantages.

2. Mathematical analysis

2.1. Equivalent modeling and state space equations

The ECM composed of electrical components is used to characterize these nonlinearities and simulate the internal impedances and polarization effects of the battery [36–38]. Considering the circuit parameter characterization effect and subsequent computational cost and complexity, in this paper, a first-order Thevenin model (FOT-ECM) is constructed to simulate electrical behavior and characterize the dynamics of the LIBs, as shown in Fig. 1.

Fig. 1. FOT-ECM.

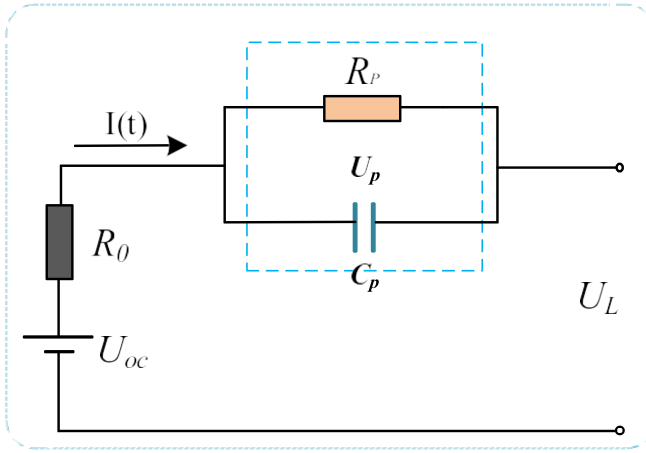

Where the R_0 is the internal ohmic resistance, R_p is the electrochemical polarization resistance, and C_p is the electrochemical polarization capacitance. The parameter of U_p is the polarization voltage, I is the charge-discharge current, U_{oc} is the open-circuit voltage, U_L is the terminal voltage, and U_o is the voltage across the ohmic resistance. The electrical behavior of the established FOT-ECM is obtained based on Kirchhoff's circuit law, as shown in Eq. (1).

$$\begin{cases} U_L = U_{oc} - U_o - U_p \\ I = C_p \dfrac{dU_p}{dk} + \dfrac{U_p}{R_p} \end{cases} \tag{1}$$

The ratio of the remaining capacity to the nominal capacity of the battery is termed for the SOC estimation. Its mathematical expression is obtained using the Ah integral method, as shown in Eq. (2).

$$SOC_t = SOC_0 - \int_0^t \frac{\eta \bullet I(t)dt}{3600 \bullet Q_n} \tag{2}$$

In Eq. (2), Q_n represents the nominal capacity of the battery and $I(k)$ represents the charging and discharging load current of the battery at time point k. With the OCV, which is usually a function of the SOC, the state-space model is established based on the FOT-ECM, as show in Eq. (3).

$$\begin{cases} \begin{bmatrix} SOC_{k+1} \\ U_{p,k+1} \end{bmatrix} = \begin{bmatrix} 1 & 0 \\ 0 & e^{-\frac{\Delta k}{\tau_1}} \end{bmatrix} \begin{bmatrix} SOC_k \\ U_{L,k} \end{bmatrix} + \begin{bmatrix} -\dfrac{\Delta k}{Q_n} \\ R_p\left(1 - e^{-\frac{k}{\tau}}\right) \end{bmatrix} I_k + \begin{bmatrix} w_{1,k} \\ w_{2,k} \end{bmatrix} \\ U_{L,k+1} = U_{oc,k} - I_k R_{0,k} - U_{p,k} + v_k \end{cases} \tag{3}$$

In Eq. (3), Δk is the sampling interval, w is the system noise, and v is the measurement noise. τ is the polynomial coefficient, and its calculation is expressed as $\tau = R_p C_p$.

2.2. FOT -ECM-based modeling with LMRLS parameter identification

The RLS method can achieve the adaptive identification of model parameters by constantly revising and updating the system parameters to accurately obtain the real-time characteristics of the system [39,40]. It has a wide range of applications in the field of system identification. The equation form of the parameters to be identified in the RLS principle is shown in Eq. (4).

$$y(k) = \phi(k)\theta(k)^T + e(k) \tag{4}$$

In Eq. (4), $y(k)$ is the output value of the system at time k, $\phi(k)$ is the observation vector, $\theta(k)$ is the parameter vector to be estimated, and $e(k)$ is the noise observation vector.

The RC network's equation is discretized to adaptively update the model parameters at each sampling time point, as shown in Eq. (5).

$$C_p\frac{U_p(k)-U_p(k-T)}{T}=I-\frac{U_p(k)}{R_p} \tag{5}$$

In Eq. (5), T is the sampling interval. The discrete equation of the ECM is obtained, as shown in Eq. (6).

$$\begin{cases} U_L(k)=U_{oc}(k)-U_p(k)-U_o(k) \\ U_L(k)=\dfrac{R_PC_P}{R_PC_P+1}U_L(k-T)+\left(R_0+\dfrac{R_PT}{R_PC_P+1}\right)I(k)-\left(\dfrac{R_0R_PC_P}{R_PC_P+1}\right)I(k-T) \end{cases} \tag{6}$$

In Eq. (6), there are three parameters R_0, R_p, and C_p to be identified in the FOT -ECM. Then, the coefficient parameter values of a_1,a_2, and a_3 are calculated and simplified as $a_1=\frac{R_pC_p}{R_pC_{p+1}}$, $a_2=R_0+\frac{R_p{}^1}{R_pC_{p+1}}$, $a_3=\frac{R_0R_pC_p}{R_pC_{p+1}}$, as shown in Eq.(7).

$$U_L(k)=a_1U_L(k-T)+a_2I(k)-a_3I(k-T) \tag{7}$$

In Eq. (7), the circuit parameters are obtained by simplifying the functional relationship between them. Therefore, the parameter to be identified is set as $\theta = [a_1, a_2, a_3]^T$. The vector form of Eq. (7) is obtained, as shown in Eq. (8).

$$\begin{cases} \varphi(k)=[U_L(k-T)\ \ I(k)\ \ I(k-T)] \\ U_L(k)=\varphi(k)\theta(k)+e(k) \end{cases} \tag{8}$$

In Eq. (8), $e(k)$ is the measurement noise with a zero-mean Gaussian white noise. In the process of parameter identification, the minimum variance criterion is used to obtain the most suitable parameters for battery characteristics and operating conditions. The criterion function J is shown in Eq. (9).

$$J=\sum\nolimits_1^N e(k)^2=(U_L-\varphi\theta)^T(U_L-\varphi\theta) \tag{9}$$

In Eq. (9), the parameter of the criterion function J is the least, which satisfies the required condition, as shown in Eq. (10).

$$\begin{cases} \dfrac{\partial J}{\partial\widehat{\theta}}=-2\varphi^{\mathrm{T}}(U_L-\varphi\widehat{\theta})=0 \\ \widehat{\theta}_{LS}=(\varphi^{\mathrm{T}}\varphi)^{-1}\varphi^{\mathrm{T}}U_L \end{cases} \tag{10}$$

From Eq. (10), θ_{LS} represents the parameter vector to be estimated under the least square method. To adapt to different conditions, the parameters are updated iteratively. From the sampled results obtained at each sampling interval, a recursive method for parameter identification based on the minimum variance theory is obtained, the forgetting factor recursive least square (FFRLS) recursive least squares method is obtained, as shown in Eq. (11).

$$\begin{cases} \widehat{\theta}(k+1)=\widehat{\theta}(k)+K(k+1)\left[y(k+1)-\phi^T(k+1)\widehat{\theta}(k)\right] \\ K(k+1)=P(k+1)\phi(k+1)\left[\phi^T(k+1)P(k)\phi(k+1)+\lambda\right]^{-1} \\ P(k+1)=\lambda^{-1}\left[I-K(k+1)\phi^T(k+1)\right]P(k) \end{cases} \tag{11}$$

In Eq. (11), λ is the forgetting factor used to prevent data saturation from causing untimely updates, and the general value is [0.95, 0.99]. λ is introduced to weaken the influence of old data and enhance the feedback effect of new data. Although FFRLS improves the shortcomings of RLS to some extent, there is still data supersaturation when there is too much data. Given the defects and deficiencies of the RLS algorithm and FFRLS algorithm, this paper designed the LMRLS, that is, when the input of new data, removes the old data, only uses the limited length of the latest data for parameter estimation [41,42]. Therefore, the LMRLS algorithm can effectively reduce the computational effort to improve the computational speed and accuracy and is more suitable for the estimation of time-varying parameters. Let the memory length of LMRLS be L, and the recursive flow is as follows.

Step1: Calculate the parameter estimate of memory length L

$$\begin{cases} \widehat{\theta}(k+1)=\widehat{\theta}(k)+K(k+1)\left[y(k+1)-\phi^T(k+1)\widehat{\theta}(k)\right] \\ K(k+1)=P(k+1)\phi(k+1)\left[\phi^T(k+1)P(k)\phi(k+1)+1\right]^{-1} \\ P(k+1)=\left[H-K(k+1)\phi^T(k+1)\right]P(k) \end{cases} \tag{12}$$

Step2: Calculate the parameter estimate of length $L+1$ at time k

$$\begin{cases} \widehat{\theta}(k-L,k)=\widehat{\theta}(k-L,k-1)+K(k-L,k)\left[y(k)-\phi^T(k)\widehat{\theta}(k-L,k-1)\right] \\ K(k-L,k)=P(k-L,k-1)\phi(k)\left[\phi^T(k)P(k-L,k-1)\phi(k)+1\right]^{-1} \\ P(k-L,k)=\left[H-K(k-L,k)\phi^T(k)\right]P(k-L,k-1) \end{cases} \tag{13}$$

Step3: Calculate the parameter estimate of length L at time k

$$\begin{cases} \widehat{\theta}(k-L+1,k) = \widehat{\theta}(k-L,k) - K(k-L+1,k)\left[y(k-L) - \phi^T(k-L)\widehat{\theta}(k-L,k)\right] \\ K(k-L+1,k) = P(k-L,k)\phi(k-L)\left[\phi^T(k-L)P(k-L,k)\phi(k-L)+1\right]^{-1} \\ P(k-L+1,k) = \left[H + K(k-L+1,k)\phi^T(k-L)\right]P(k-L,k) \end{cases} \tag{14}$$

where K (*) is the gain function, P (*) is the covariance function, and H is the unit matrix. Where, $\theta(k-L, k-1)$ represents the parameter identification result corresponding to the L set of data from the moment k-L to moment k-1, $\theta(k-L, k)$ denotes the parameter identification result corresponding to the $L+1$ set of data from the moment k-L to moment k, $\theta(k-L+1,k)$ stands for the parameter identification result corresponding to the L set of data from the moment k-$L+1$ to moment k.

The identification of the characteristic parameters of the battery at each SOC level is based on the existing experimental data and the established FOT -ECM. The wide application of LIBs determines the complexity of the working conditions. The active internal electrochemical characteristics of the battery are greatly influenced by the present SOC value, charge-discharge current rates, ambient temperatures, etc., which are constantly changing. In this paper, the LMRLS online parameter identification is conducted to identify the parameters of the battery with time-varying parameter characterization, which is more convenient and accurate than the offline procedure. It obtains more accurate values for the time-varying characteristic parameters by continuously correcting and updating the system. The flowchart of the adaptive updating parameter identification method for the battery model is shown in. Fig. 2.

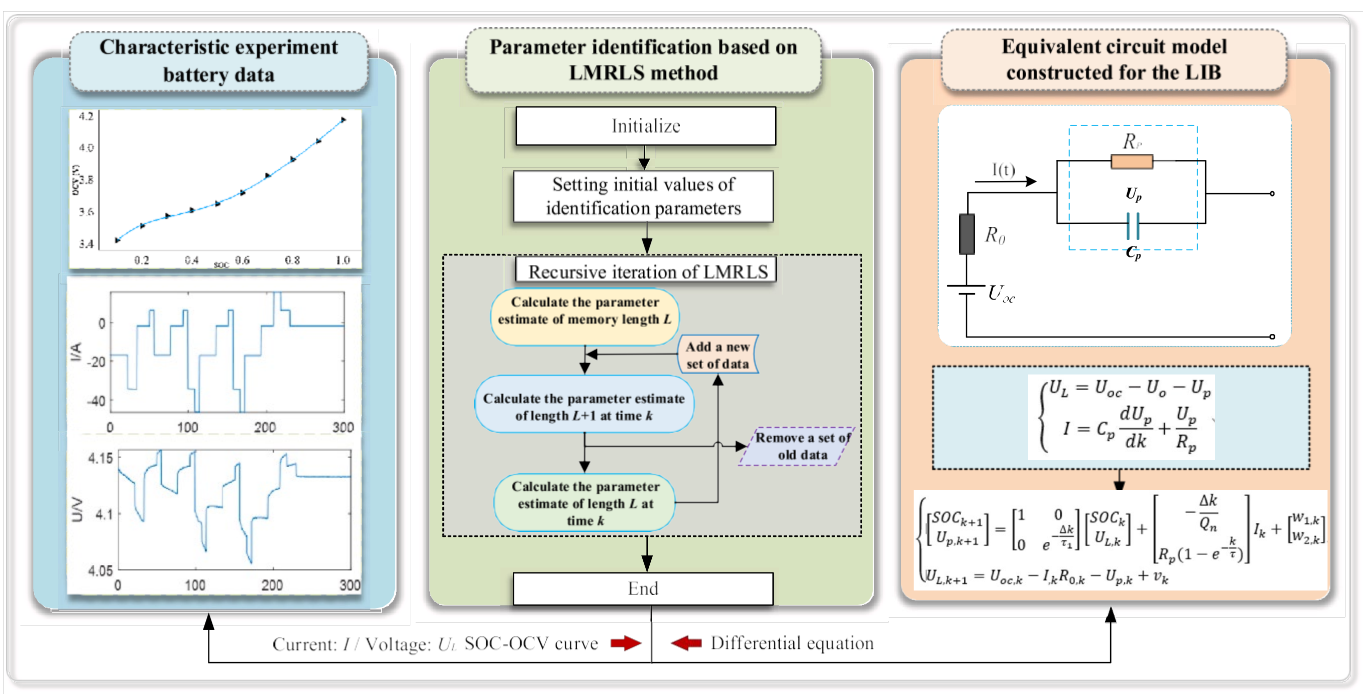

Fig. 2. Flowchart of the adaptive online parameter identification method.

2.3. Iterative RBC-DSVM-based parameter calculation

As a system with highly nonlinear characteristics and multi-dimensional space, the SOC of LIBs is affected by many external factors, which increases the difficulty of real-time estimation. To solve this problem, the discrete-time domain state-space equation is established. At each discrete sampling point, SOC and battery capacity are regarded as two circuit links in system state variable prediction and correction to improve the robustness of the system. The state-space and measurement equations of the discrete nonlinear system are shown in Eq. (15).

$$\begin{cases} x_{k|k-1} = f(x_{k-1}, u_k) + \omega_k \\ y_k = g(x_k, u_k) + \nu_k \end{cases} \tag{15}$$

In Eq. (15), x_k is the state-transition matrix, u_k is the control-input vector, and y_k is the measurement matrix. $f(x_k, u_k)$ is a nonlinear state function of the system, which represents the cumulative change of state parameters under the effect of the input vector u_k, and $g(x_k, u_k)$ is a nonlinear measurement equation of the system. The nonlinear function is linearized by a first-order Taylor series expansion around the filtering value, as shown in Eq. (16).

$$\begin{cases} A_k = \dfrac{\partial f(x_k, u_k)}{\partial x_k} | x_k = \widehat{x}_k \\ B_k = \dfrac{\partial g(x_k, u_k)}{\partial x_k} | x_k = \widehat{x}_k \end{cases} \tag{16}$$

In Eq. (16), the coefficients are calculated to obtain the nonlinear equation after linearization, as shown in Eq. (17).

$$\begin{cases} f(x_k, u_k) = f(\widehat{x}_k, u_k) + \dfrac{\partial f(x_k, u_k)}{\partial x_k} | x_k = \widehat{x}_k (x_k - \widehat{x}_k) \\ g(x_k, u_k) = g(\widehat{x}_k, u_k) + \dfrac{\partial g(x_k, u_k)}{\partial x_k} | x_k = \widehat{x}_k (x_k - \widehat{x}_k) \end{cases} \tag{17}$$

In Eq. (17), x_k is the estimated value of the state vector at the time point k. After linearizing the space-state equation, the nonlinear sysem's state-space and measurement equations are obtained, as shown in Eq. (18).

$$\begin{cases} x_{k+1} = \widehat{A}_k x_k + [f(\widehat{x}_k, u_k) - \widehat{A}_k x_k] + \omega_k \\ y_k = \widehat{C}_k x_k + [g(\widehat{x}_k, u_k) - \widehat{C}_k x_k] + \nu_k \end{cases} \tag{18}$$

In Eq. (18), the nonlinear system is subjected to iterative filtering processing through the linearization processing described. The specific iterative steps are expressed as follows: (1) Initialization of state vari- ables and the error covariance matrix; (2) Time update of the prior state estimate; (3) Time update of the prior error covariance matrix; (4) Up-date of the Kalman gain; (5) Measurement update of the posterior state estimate; (6) Measurement update of the posterior error covariance matrix. The corresponding calculation equations are defined, as shown in Eq. (19).

$$\begin{cases} (1)\ \hat{x}_{0|0} = E(x_0)\ ,\ P_{0|0} = var(x_0) \\ (2) \widehat{x}_{k+1|k} = A_{k-1}\widehat{x}_{k|k-1} + B_{k-1}u_{k-1} + q_k \\ (3) P_{k+1|k} = E\left[(x_k - \widehat{x}_{k|k-1})(x_k - \widehat{x}_{k|k-1})^T\right] = A_{k-1}P_{k|k-1}{A_{k-1}}^T + Q_{k-1} \\ (4)\ K_k = P_{k|k-1}C_k^T\left(C_k P_{k|k-1}{C_k}^T + R_k\right)^{-1} \\ (5) \widehat{x}_{k|k} = \widehat{x}_{k|k-1} + K_k(y_k - C_k\widehat{x}_{k|k-1} - D_k u_k - r_k) \\ (6) P_{k|k} = (E - K_k C_k)P_{k|k-1} \end{cases} \tag{19}$$

In Eq. (19), $x_{0|0}$ and $P_{0|0}$ are the initial values of the system state and error covariance matrix, respectively. $x_{k+1|k}$ is the estimated value of the state parameter vector at time point $k + 1$, $x_{k|k-1}$ is the estimated value of the state parameter vector at time point k, $P_{k|k-1}$ is the priori error covariance matrix, $P_{k+1|k}$ is the posteriori error covariance matrix. After the system is initialized, the filter estimation value of each sampling point is updated recursively. The goal of time-series problems is to estimate the state quantity and error covariance at the previous time based on the filtered value and input quantity at the previous time.

The measurement update is based on the observed value outside the system. The state estimate value and error covariance matrix update under the system noise are considered for correction to obtain the optimal estimation in the sense of minimum variance. The obtained optimal filter value is used as the input when updating the time at the next moment to realize a recursive "prediction and correction" iteration. The system is initialized first with its variables, as shown in Eq. (20).

$$\begin{cases} \widehat{X}_k = E(X_0) \\ P_k = E(X_0 - \widehat{X}_k)(X_0 - \widehat{X}_k)^T \end{cases} \tag{20}$$

In Eq. (20), X_k is the estimated value using the initial state variable and P_k is the error covariance matrix. Then, the time update of the Kalman gain K is performed with the error covariance matrix, as shown in Eq. (21).

$$\begin{cases} \widehat{P}_k = A_k P_k A_k^T + Q_k \\ K_{k+1} = \widehat{P}_{k+1} C_{k+1}^T \left(C_{k+1}\widehat{P}_{k+1}C_{k+1}^T + R_{k+1}\right)^{-1} \end{cases} \tag{21}$$

In Eq. (21), the Kalman gain matrix is obtained by combining the difference between the real-time data and system observation data, which corrects the prior estimate. If the difference is large, the state variable is recursively updated accordingly, as shown in Eq. (22).

$$\begin{cases} x_{k+1} = \widehat{x}_{k+1} + K_{k+1}(y_{k+1} - C_{k+1}\widehat{x}_{k+1} - D_{k+1}u_{k+1}) \\ P_{k+1} = (E - K_{k+1}C_{k+1})\widehat{P}_{k+1} \end{cases} \tag{22}$$

In Eq. (22), the adaptive update of SOC is achieved by estimating and correcting the time-varying characteristics of the process noise and the measurement noise of the system, as shown in Eq. (23).

$$\begin{cases} q_k = (1 - d_{k-1})q_{k-1} + d_{k-1}G(\widehat{x}_k - A\widehat{x}_{k-1} - Bu_{k-1}) \\ Q_k = (1 - d_{k-1})Q_{k-1} + d_{k-1}G\left(L_k\overline{y}_k\overline{y}_k^T L_k^T + P_k - AP_{k|k-1}A^T\right)G^T \\ r_k = (1 - d_{k-1})r_{k-1} + d_{k-1}(y_k - C\widehat{x}_{k|k-1} - Du_{k-1} - d) \\ R_k = (1 - d_{k-1})R_{k-1} + d_{k-1}\left(\overline{y}_k\overline{y}_k^T - CP_{k|k-1}C^T\right) \end{cases} \tag{23}$$

Maximizing the interval between support vectors, the improved RBC-DSVM finds the maximum interval to the hyperplane for the training dataset, which is the maximum interval principle, optimizing the distance to the farthest sample point from the hyperplane. First, a training dataset is sampled as $\{(x_i, y_i)|i = 1, 2, 3, \ldots, n\}, x_i \in R_n$, where x_i is the ith m-dimensional input vector and y_i is the corresponding output vector. $f(x) = sign\,(w^*x + b)$ is the hyperplane found. The conditions are to be satisfied by this hyperplane, as shown in Eq. (24).

$$d \le \frac{\varepsilon}{\sqrt{1 + \| w \|}} \tag{24}$$

In Eq. (24), the relationship is used as the basic convergence law of the iterative calculation process. Then, the optimization target of the SVM is realized, as shown in Eq. (25).

$$\begin{cases} min\frac{1}{2}w^T w \\ s.t.|f(x) - y_i| \le \varepsilon, i = 1, 2, \ldots, m \end{cases} \tag{25}$$

In Eq. (25), if most of the data in the original space cannot be partitioned, the original data is mapped to a higher dimensional space using the kernel function. Inevitably, there will be sample points that do not fall into the sample points in the actual use of the process. The solution to this problem is to introduce a loss function l_z after the introduction of the loss function SVM optimization target, as shown in Eq. (26).

$$\begin{cases} min\frac{1}{2}w^T w + C\sum_{i=1}^{N} l_z(f(x_i) - y_i) \\ s.t.|w^T \bullet \Phi(x) + b - y_i| \le \varepsilon, i = 1, 2, \ldots, m \end{cases} \tag{26}$$

In Eq. (26), $\Phi(x)$ is the kernel function, and C is the regularization constant, which is a fixed value and has an effect on the model's complexity. ε is the approximate accuracy of the training samples, which controls the number of support vectors. After introducing the relaxation variables ξ_i, and ξ_i^*, Eq. (26) is optimized, as shown in Eq. (27).

$$\begin{cases} min\frac{1}{2}w^T w + C\sum_{i=1}^{N}(\xi_i + \xi_i^*) \\ y_i - (w \bullet \Phi(x) + b) \le \varepsilon + \xi_i \\ w \bullet \Phi(x) + b - y_i \le \varepsilon + \xi_i^* \\ \xi_i\xi_i^* \ge 0 \end{cases} \tag{27}$$

In Eq. (27), since the battery is a nonlinear system, a nonlinear RB kernel function is introduced, as shown in Eq. (28).

$$\begin{cases} K(x, x_i) = \Phi(x)^*\Phi(x_i) \\ f(x) = \sum_s (a_i - a_i^*)K(K(x, x_i)) + b \end{cases} \tag{28}$$

The final nonlinear regression equation after the introduction of the nonlinear RBC of the kernel is $K(x, x_i)$, where s is the number of support vectors.

2.4. RBC-DSVM-based optimization and correction

The improved RBC-DSVM method is constructed with the Vapnik-Chervonenkis (VC) dimensional statistical learning and structural risk minimization, which enables the statistical noise characteristics in the filtering method to be updated adaptively. The RBC-DSVM model is proposed to correct and optimize the accurate final SOC estimation. The flowchart of the proposed RBC-DSVM-based SOC estimation is presented in Fig. 3.

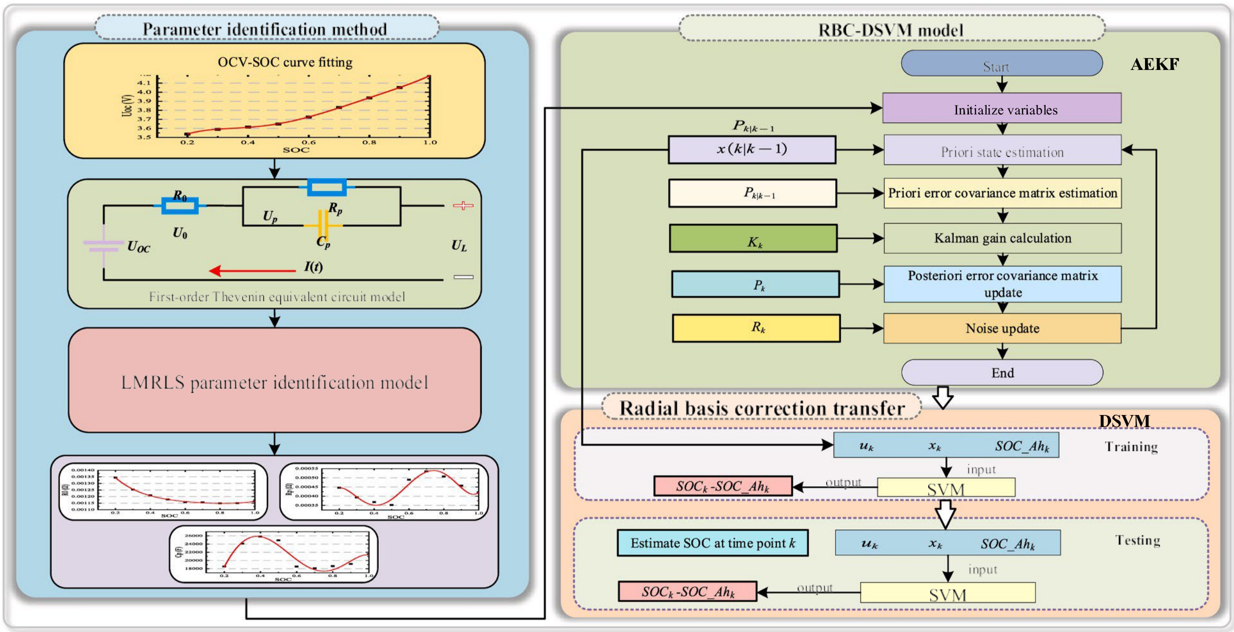

Fig. 3. The flowchart of the RBC-DSVM model for battery state estimation.

In Fig. 3, the specific model implementation steps are to first train a three-input, one-output (x_k), using the RB kernel function, the input variables are the voltage value U_k at time point k, and the SOC estimate s(k). The SOC value $socah_k$ estimated by the Ah integration method, and the output is the estimation error $s(k)-\hat{s}(k)$. The training datasets are divided according to 7:3, which is 70 % as training data and 30 % as validation data.

3. Experimental methods and effect verification

3.1. Experimental test platform construction

An experimental platform is established for LIB tests to obtain real-time data under various working conditions to test and verify the proposed method. After constructing the structural battery principles, OCV is the LIB's voltage for no-load and no-power supply conditions. The relevant experiments are conducted for the actual working conditions to obtain experimental data. The LIB's test platform provides a stable working environment, and the upper computer is used to set the required steps of various working conditions. The high-power charge-discharge tester records the current, voltage, temperature, etc., of the battery during its operation at a time interval of 0.1 s.

For the research object, an LNCM50Ah (lithium nickel cobalt manganese oxide) LIB is used. It has a nominal capacity and voltage of 50 Ah and 3.7 V, respectively. It has a nickel-cobalt manganese cathode electrode and a natural graphite anode electrode with a metallic backing. The LIB's basic technical specifications are shown in Table 1.

Table 1
Basic technical information about the experimental LIB cells.

Parameter	Value	Parameter	Value
Normal capacity	50 Ah	Standard charge current	1C
Normal voltage	3.65 V	Maximum discharge current	5C
Charge cut-off voltage	4.5 ± 0.05 V	Internal resistance	0.8 mΩ
Discharge cut-off voltage	2.5 ± 0.05 V	Dimensions: l × w × h	148 × 27 × 93 (mm)

For the experimental tests, the NEWARE battery test equipment (CT- 4016) is used. It has a maximum current of 100 A, a voltage range of 25–100 V, and a maximum charge and discharge power of 12.4 kW. The temperature testing equipment is a DGBELL BTT−331C, which maintains the battery's temperature at 25 °C during its operation. The entire experimental test platform is primarily comprised of a computer for configuring, monitoring, and storing the test data for each operating condition. It also includes the primary battery testing equipment for charging and discharging the battery, a functioning LIB, and a temperature test chamber for controlling and stabilizing the battery's working temperature.

3.2. Parameter identification and experimental verification

With time, the aging phenomenon of LIBs occurs, which is characterized by the gradual change of battery capacity, internal resistance, polarization resistance, and other parameters. To establish the coupling relationship among the parameters to extract the aging characteristics of the battery, intermittent discharge tests, and aging tests are conducted for LIBs. After every 100 aging tests, OCV, SOC, and capacity data are extracted to establish the capacity-OCV-SOC coupling relationship, as shown in Fig. 4.

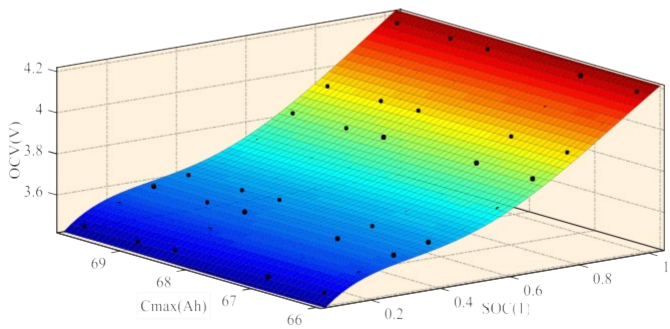

Fig.4. Fitting diagram of battery coupling information with *Qmax*-OSV-SOC fitting relationship.

In Fig. 4, through a large number of tests on LIBs, it is found that the OCV-SOC function of LIBs is not constant in the process of use. With the aging process, its indicators will change, and several aging characteristics need to be extracted to characterize the changes in the health status of the LIB. Multi-parameter fitting polynomials are used to minimize the variance between the capacity, OCV, and SOC values of the LIB are established, as shown in Eq. (29).

$$\begin{aligned} Z &= \mathrm{P}_{00} + \mathrm{P}_{01}\mathrm{y} + \mathrm{P}_{02}\mathrm{y}^2 + \left(\mathrm{P}_{10} + \mathrm{P}_{11}\mathrm{y} + \mathrm{P}_{12}\mathrm{y}^2\right)\mathrm{x} + \left(\mathrm{P}_{20} + \mathrm{P}_{21}\mathrm{y} + \mathrm{P}_{22}\mathrm{y}^2\right)\mathrm{x}^2 \\ &= + \left(P_{30} + P_{31}y + P_{32}y^2\right)x^3 + (P_{40} + P_{41}y)x^4 + P_{50}x^5 \end{aligned} \tag{29}$$

In Eq. (29), x represents the estimated SOC, y represents the maximum available capacity Q_{max}, and Z represents the OCV. Based on the empirical formula, x is designed as a fifth-order polynomial, and y is a second-order polynomial. The final coefficient values of the OCV, SOC, and Qmax are shown in Table 2.

Table 2

Final coefficient values of the OCV, SOC, and Qmax of the LIB cells.

P_{00}	P_{01}	P_{02}	P_{10}	P_{11}
−2.605	0.1793	−0.001365	32.47	−0.9279

P_{12}	P_{20}	P_{21}	P_{22}	P_{30}
0.00718	−71.1	1.971	−0.01551	50.93

P_{31}	P_{32}	P_{40}	P_{41}	P_{50}
−1.182	0.009637	−8.577	−0.03275	2.828

By establishing the coupling function relationship between $Q_{\max}$, OCV, and SOC, accurate observation equations are obtained to update and correct the SOC estimation results. Various battery test conditions that conform to the vehicle's operating conditions are very necessary. The complex working condition experiments in this section mainly include the HPPC test, DST test, and Beijing bus dynamic stress test (BBDST).

The experimental data is used subsequently for verification of the established FOT-ECM and state estimation. The FOT-ECM parameter values fluctuate due to factors such as aging level, SOC value, and charge-discharge current rate. The model parameters are updated adaptively based on the LMRLS method by using actual working condition datasets. Also, to eliminate the influence of the aging phenomenon on the battery, the OCV is corrected to realize the optimal characterization of the internal characteristics of the battery. The parameter identification results and the observed voltage error under the HPPC working condition are obtained, as shown in Fig. 5.

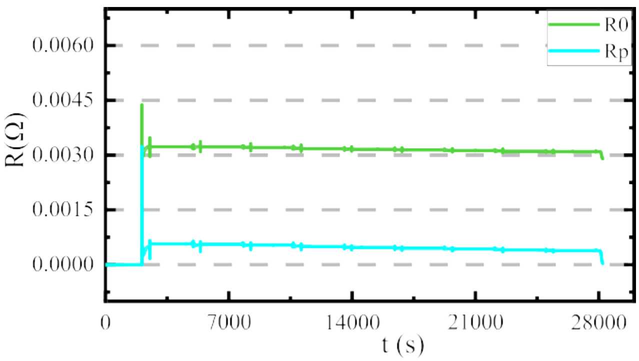

(a) Time-varying ohmic and electrochemical resistance curves

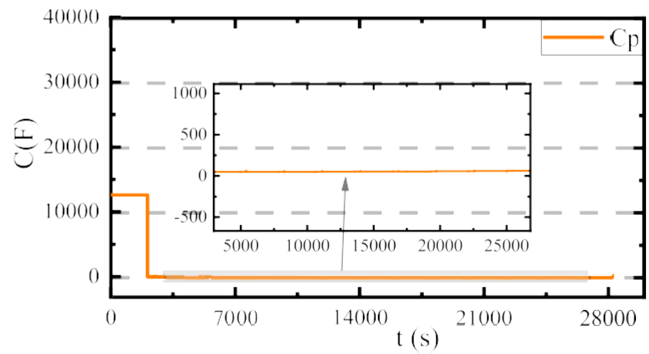

(b) Time-varying electrochemical capacitance a

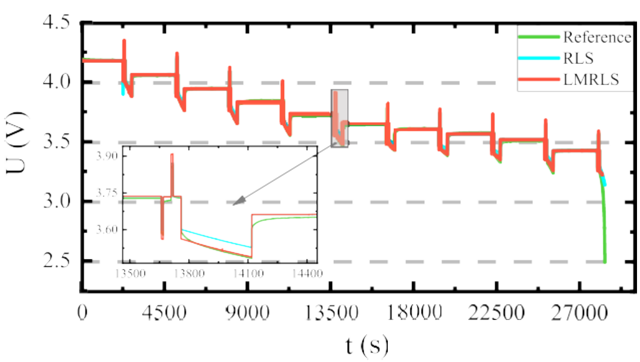

(c) Voltage comparison curve under the HPPC condition

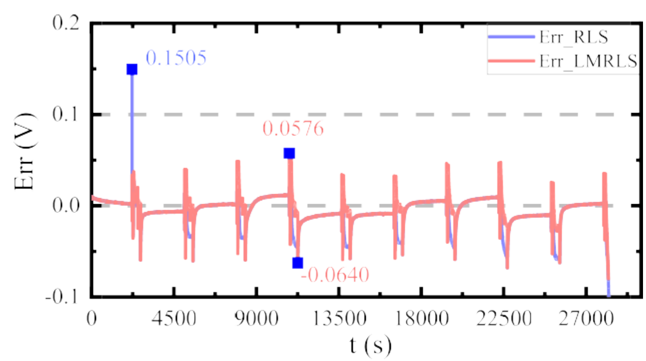

(d) Voltage traction error curve under the HPPC condition

Fig. 5. Time-varying parameter identification and voltage traction error curves of the FOT –ECM.

In Fig. 5, subfigure (a) is the identified change curves of ohmic resistance R_0 and polarization resistance R_p, and subfigure (b) is the identified change curve of C_p. In subfigure (c), the time-varying result for the output voltage is obtained by comparing the actual voltage with the simulated voltage. By comparing the actual voltage and the simulated output, it can be observed that the simulated voltage by the LMRLS tracks the actual voltage variation of the LIB well, with a maximum error value of 0.064 V, as shown in subfigure (d). Especially at the moment of voltage abrupt change, the tracking ability is superior to RLS. And the overall error curve of LMRLS fluctuates less in the whole process. By critically analyzing the error curves, an increased margin error is observed at the latter stage of the traction process due to the drift of the load current at the end of the discharge cycles, which is an inherent limitation of the LIB.

3.3. RBC-DSVM-based SOC estimation under the HPPC working condition

The HPPC and DST working conditions are conducted as the test conditions to simulate the actual operating conditions of the LIB, verifying that the proposed RBC-DSVM model has good accuracy and adaptability under different working conditions. The SOC is estimated with voltage variation characteristics. The actual SOC is input into the RBC-DSVM model for training. The SOC estimation results under the HPPC working condition are shown in Fig. 6.

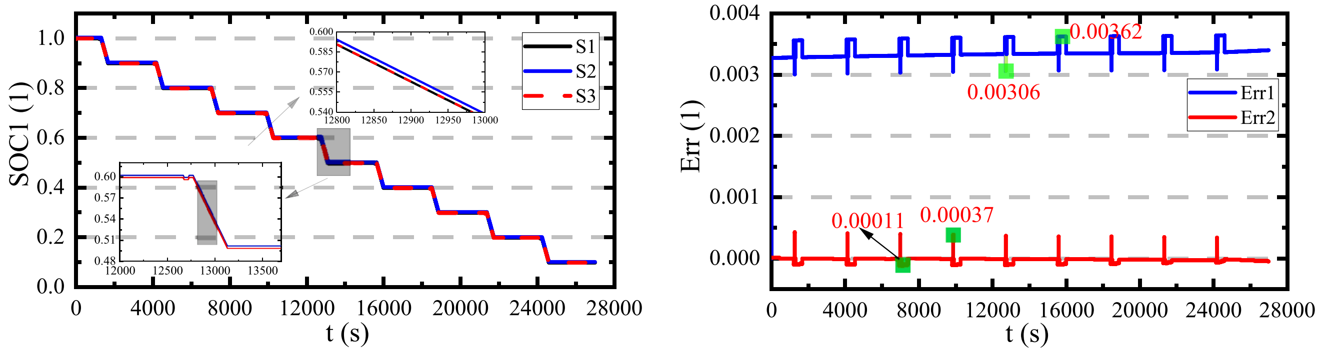

(a) SOC estimation curves

(b) Estimation error curves

Fig. 6. SOC estimation results under the HPPC working condition.

Fig. 6(a) presents the SOC estimated by the constructed model, where $S1$ represents the actual SOC of the battery system, which is obtained by the Ah integration method. $S2$ represents the SOC estimated by the AEKF method, and $S3$ represents the SOC estimated by the RBC- DSVM model. Fig. 6(b) represents the SOC estimation error, where $Err1$ represents the SOC estimation error of the AEKF method, and $Err2$ represents the SOC estimation error of the RBC-DSVM model. Comparing the two estimation results, it can be observed that the AEKF method has a maximum error of 0.362 %, and that of the proposed RBC- DSVM model is 0.037 %. The adaptability of the estimation of the RBC- DSVM model by showing stability to the actual SOC for the entire estimation process makes it robust and optimal compared to the AEKF method.

3.4. RBC-DSVM-based SOC estimation under the DST working condition

To further verify the accuracy and robustness of the proposed RBC- DSVM model, the SOC estimation is carried out under the DST working condition. The SOC estimation results are shown in Fig. 7.

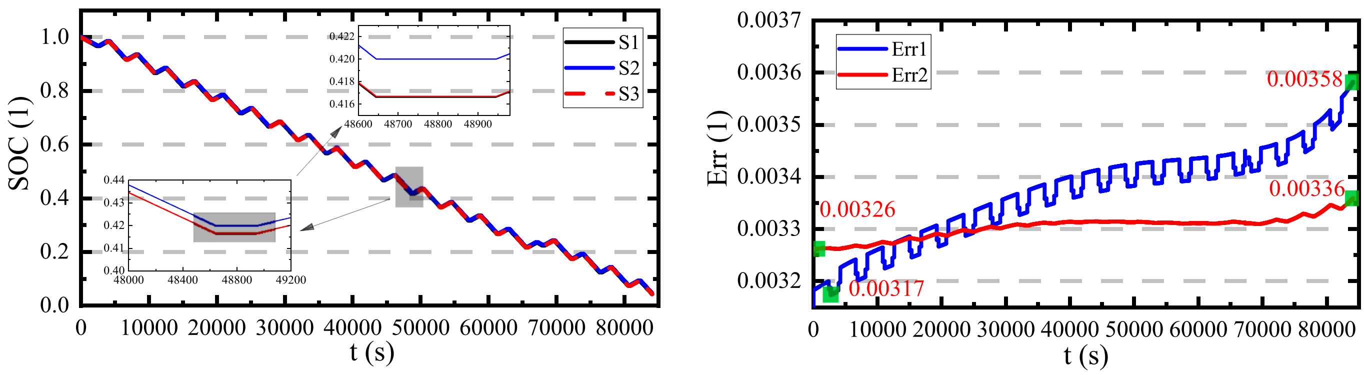

(a) SOC estimation curves

(b) Estimation error curves

Fig. 7. SOC estimation results under the DST working condition.

Fig. 7(a) presents the SOC estimation results under the DST working condition, where $S1$ is the actual SOC estimated of the battery system, which is obtained by the Ah integral method. $S2$ is the SOC estimated by the AEKF method, and $S3$ is the SOC estimated by the RBC-DSVM model. Fig. 7(b) shows a plot of the SOC estimation errors, where $Err1$ is the error curve of the SOC estimated by the AEKF method, and $Err2$ is the error curve of the SOC estimated by the RBC-DSVM model. It can be observed that the maximum error of the AEKF method is 0.358 %, while the RBC-DSVM model has a maximum error of 0.336 %. Also, the error of the AEKF method shows a monotonic increasing order, while the error fluctuation of the RBC-DSVM model is significantly less compared to the AEKF method, which verifies its robustness and accuracy.

4. Conclusion

As the technical bottleneck of the development of pure electric new energy vehicles, the performance level of power batteries directly affects the performance of pure electric vehicles. SOC is a critical state quantity that must be accurately evaluated in a battery management system and is a necessary prerequisite for the effective realization of functions such as balance control, charge/discharge strategy adjustment, and fault diagnosis. To achieve an accurate evaluation of power battery SOC, this paper designed LMRLS online parameter identification method based on FOT-ECM and established the RBC-DSVM model. By establishing the coupling function relationship between Q_{max}, OCV, and SOC to obtain accurate observation equations. The SOC estimation is further corrected and optimized by inputting it into a proposed RBC-DSVM model.

To verify the accuracy and robustness of the proposed RBC-DSVM model, SOC estimation effect analysis is conducted under different working conditions. The estimation results show that the proposed RBC- DSVM model has a maximum error of 0.037 % and 89.78 % performance improvement compared to the AEKF method under the HPPC working condition. Additionally, under the DST working condition, the proposed RBC-DSVM model shows a maximum error of 0.336 % and a 6.15 % performance improvement compared to the AEKF method. Therefore, the proposed RBC-DSVM model can accurately estimate the SOC in real- time applications. This lays the foundation for state estimation of LIBs under various working conditions.

However, there are still some details that need to be improved and optimized in this study.

(1) SOC evaluation time and computational complexity need to be seriously considered and solved. The estimation time and computational complexity of SOC are related to the efficiency and security of BMS. However, at present, there is no unified evaluation index for evaluation time and computational complexity, and it is difficult to verify computational complexity.

(2) The performance under noise and parameter uncertainty needs to be further verified. The working conditions and environment in reality are often complex and variable. The data in this study come from the working conditions designed in the laboratory, which have some deviation from the operating conditions of electric vehicles in reality and fail to consider the problems of noise and various changing parameters issues well.

(3) The influence of different temperature and state noise needs to be further considered. In reality, ambient temperature and noise change from time to time, so it is necessary to consider the influence of time-varying temperature and state noise.

Given the above limitations of this study, the author will carefully consider and address them in future research work. For example, the use of real vehicle data is considered to further validate the methodology proposed in this study, and the program of this study will be improved based on the validation results.

CRediT authorship contribution statement

Shunli Wang: Conceptualization, Methodology, Project administration, Software, Supervision, Writing – original draft. **Chao Wang:** Data curation, Software, Visualization, Writing – original draft, Writing – review & editing. **Paul Takyi-Aninakwa:** Methodology, Supervision, Validation, Writing – original draft, Writing – review & editing. **Siyu Jin:** Software, Validation. **Carlos Fernandez:** Writing – review & editing. **Qi Huang:** Writing – review & editing.

Declaration of competing interest

The authors declare that they have no known competing financial interests or personal relationships that could have appeared to influence the work reported in this paper.

Data availability

All data included in this study are available upon request by contact with the corresponding author.

Acknowledgment

The work is supported by the National Natural Science Foundation of China (No. 62173281, 52377217, U23A20651), the Sichuan Science and Technology Program (No. 23ZDYF0734, 23NSFSC1436), and the Fund of Robot Technology used for Special Environment Key Laboratory of Sichuan Province (No. 18kftk03). Thanks to the sponsors. Carlos Fernandez also expresses his profound gratitude to Robert Gordon University for its support.

References

[1] W. Wang, L.W. Fan, P. Zhou, Evolution of global fossil fuel trade dependencies, Energy 238 (2022) 1–12.

[2] J. Zhu, et al., An improved electro-thermal battery model complemented by current dependent parameters for vehicular low temperature application, Appl. Energy 248 (2019) 149–161.

[3] L.S. Martins, et al., Electric car battery: an overview on global demand, recycling and future approaches towards sustainability, J. Environ. Manage. 295 (2021) 1–16.

[4] C. Liao, et al., Magnetron sputtering deposition of silicon nitride on polyimide separator for high-temperature lithium-ion batteries, J. Energy Chem. 56 (2021) 1–10.

[5] Z. Wei, et al., Online estimation of power capacity with noise effect attenuation for lithium-ion battery, IEEE Trans. Ind. Electron. 66 (7) (2019) 5724–5735.

[6] J. Tian, R. Xiong, W. Shen, State-of-health estimation based on differential temperature for lithium ion batteries, IEEE Trans. Power Electron. 35 (10) (2020) 10363–10373.

[7] P. Shen, et al., The co-estimation of state of charge, state of health, and state of function for Lithium-ion batteries in electric vehicles, IEEE Trans. Veh. Technol. 67 (1) (2018) 92–103.

[8] G.S. Misyris, et al., State-of-charge estimation for li-ion batteries: a more accurate hybrid approach, IEEE Trans. Energy Convers. 34 (1) (2019) 109–119.

[9] Y.J. Wang, Z.H. Chen, A framework for state-of-charge and remaining discharge time prediction using unscented particle filter, Appl. Energy 260 (2020), 114324.

[10] W.H. Xu, et al., A novel adaptive dual extended Kalman filtering algorithm for the li-ion battery state of charge and state of health co-estimation, Int. J. Energy Res. 45 (10) (2021) 14592–14602.

[11] P.P. Xu, et al., Adaptive state-of-charge estimation for lithium-ion batteries by considering capacity degradation, Electronics 10 (2) (2021) 1–17.

[12] Z. Chen, et al., Particle filter-based state-of-charge estimation and remaining- dischargeable-time prediction method for lithium-ion batteries, J. Power Sources 414 (2019) 158–166.

[13] W.L. Zhou, et al., Review on the battery model and SOC estimation method, Processes 9 (9) (2021) 1–23.

[14] M. Adaikkappan, N. Sathiyamoorthy, Modeling, state of charge estimation, and charging of lithium-ion battery in electric vehicle: a review, Int. J. Energy Res. 46 (3) (2022) 2141–2165.

[15] M. Dubarry, et al., Battery energy storage system modeling: a combined comprehensive approach, J. Energy Storage 21 (2019) 172–185.

[16] Z.H. Cui, et al., A comprehensive review on the state of charge estimation for lithium-ion battery based on neural network, Int. J. Energy Res. 46 (5) (2022) 5423–5440.

[17] C. Wang, et al., A novel BCRLS-BP-EKF method for the state of charge estimation of lithium-ion batteries, Int. J. Electrochem. Sci. 17 (4) (2022) 1–17.

[18] J.H. Zhao, et al., Review of state estimation and remaining useful life prediction methods for lithium-ion batteries, Sustainability 15 (6) (2023) 1–22.

[19] X. Yang, et al., Fuzzy adaptive singular value decomposition cubature Kalman filtering algorithm for lithium-ion battery state-of-charge estimation, Int. J. Circuit Theory Appl. 50 (2) (2022) 614–632.

[20] F. Naseri, et al., An enhanced equivalent circuit model with real-time parameter identification for battery state-of-charge estimation, IEEE Trans. Ind. Electron. 69 (4) (2022) 3743–3751.

[21] J.D. Duan, et al., State of charge estimation of lithium battery based on improved correntropy extended Kalman filter, Energies 13 (16) (2020) 1–18.
[22] Y. Wang, et al., Estimation of battery open-circuit voltage and state of charge based on dynamic matrix control-extended Kalman filter algorithm, J. Energy Storage 52 (2022) 1–13.
[23] L. Zhou, et al., State estimation models of lithium-ion batteries for battery management system: status, challenges, and future trends, Batteries-Basel 9 (2) (2023) 1–23.
[24] X.T. Liu, et al., Data-driven state of charge estimation for power battery with improved extended Kalman filter, IEEE Trans. Instrum. Meas. (2023) 72.
[25] Z. Ren, C. Du, A review of machine learning state-of-charge and state-of-health estimation algorithms for lithium-ion batteries, Energy Rep. 9 (2023) 2993–3021.
[26] J.C. Hong, et al., Online joint-prediction of multi-forward-step battery SOC using LSTM neural networks and multiple linear regression for real-world electric vehicles, J. Energy Storage 30 (2020) 1–12.
[27] H.X. Tian, et al., A review of the state of health for lithium -ion batteries: research status and suggestions, J. Clean. Prod. 261 (2020) 1–30.
[28] B.Y. Liu, et al., State of charge estimation for lithium-ion batteries based on improved barnacle mating optimizer and support vector machine, J. Energy Storage 55 (2022) 1–12.
[29] N. Shi, et al., State-of-charge estimation for the lithium-ion battery based on adaptive extended Kalman filter using improved parameter identification,
J. Energy Storage 45 (2022) 1–15.
[30] Q. Zhu, et al., A state of charge estimation method for lithium-ion batteries based on fractional order adaptive extended kalman filter, Energy 187 (2019) 1–13.
[31] X. Zhao, K. Kim, S. Jung, State-of-charge estimation using data fusion for vanadium redox flow battery, J. Energy Storage 52 (2022) 1–10.
[32] R. Xiong, et al., A double-scale, particle-filtering, energy state prediction algorithm for Lithium-ion batteries, IEEE Trans. Ind. Electron. 65 (2) (2018) 1526–1538.
[33] P. Ren, et al., Novel strategy based on improved Kalman filter algorithm for state of health evaluation of hybrid electric vehicles li-ion batteries during short- and longer term operating conditions, Journal of Power Electronics 21 (8) (2021) 1190–1199.
[34] C. Wang, et al., Parameters identification of Thevenin model for lithium-ion batteries using self-adaptive particle swarm optimization differential evolution algorithm to estimate state of charge, J. Energy Storage 44 (2021) 1–18.
[35] Y. Qiu, et al., State of charge estimation of vanadium redox battery based on improved extended Kalman filter, ISA Trans. 94 (2019) 326–337.
[36] P. Huang, et al., The state of health estimation of lithium-ion batteries based on data-driven and model fusion method, J. Clean. Prod. 366 (2022).
[37] Y.J. Wang, et al., A comprehensive review of battery modeling and state estimation approaches for advanced battery management systems, Renew. Sustain. Energy Rev. 131 (2020) 1–18.
[38] S.L. Wang, et al., Improved compound correction-electrical equivalent circuit modeling and double transform-unscented Kalman filtering for the high-accuracy closed-circuit voltage and state-of-charge co-estimation of whole-life-cycle lithium- ion batteries, Energ. Technol. 10 (12) (2022).
[39] X.Y. Hao, et al., An improved forgetting factor recursive least square and unscented particle filtering algorithm for accurate lithium-ion battery state of charge estimation, J. Energy Storage 59 (2023) 1–12.
[40] X.H. Du, et al., Online identification of Lithium-ion battery model parameters with initial value uncertainty and measurement noise, Chin. J. Mech. Eng. 36 (1) (2023) 1–10.
[41] X.Y. Kong, et al., Online smart meter measurement error estimation based on EKF and LMRLS method, IEEE Trans. Smart Grid. 12 (5) (2021) 4269–4279.
[42] C. Wang, et al., A novel back propagation neural network-dual extended Kalman filter method for state-of-charge and state-of-health co-estimation of lithium-ion batteries based on limited memory least square algorithm, J. Energy Storage 59 (2023) 1–13.